Drag reduction of a transport helicopter by application of an adjoint-based fuselage optimization chain and modification of the rotor head

Marc Wentrup, Walid Khier
(Marc.Wentrup@dlr.de, Walid.Khier@dlr.de)
Institute of Aerodynamics and Flow Technology, DLR
Qinyin Zhang
(Qinyin.Zhang@eurocopter.com)
Airbus Helicopters Deutschland GmbH

March 2014

Abstract

In this paper two approaches are investigated to reduce the parasite drag of a helicopter. The first approach is to optimize the surface of the fuselage back door. This is done by applying an automatic, adjoint-based optimization chain; developed by DLR for these purposes. This optimization chain combines the RANS-solver TAU with a solver for the discrete adjoint equation and a conjugate-gradient based optimization algorithm. The parameterization is done by Free Form Deformation. A description of the functionality of the chain is given, before the results of the optimization run are presented. The resulting surfaces were able to bring benefits, up to 3.75% drag reduction compared to the baseline geometry. The second approach is to reduce the main rotor head drag, by installing a hub fairing. During this investigation, two different hub geometries were tested. By using a fully closed fairing, a drag reduction of about 19% could be achieved.

Introduction

To reduce the emission of greenhouse gases to gain more acceptances in the public and to reduce operational costs, the European research facilities, in collaboration with industrial partners, are continuously contributing to improve the efficiency of helicopters. The fuselage and the main rotor head causes together about 70% of the parasite drag on a helicopter [1]. The reduction of these losses, for several helicopter weight classes, is part of goals of the GRC2-project. In this paper the common H/C platform (NH90) will be considered.

On the fuselage, the focus is set to the back door. Its shape causes a flow separation and forms two strong trailing vortices which increase drag losses. A study of the ONERA showed that the installation of vortex generator on the backdoor could reduce the drag of about 4.7% [2]. During GRC2, the DLR task is to investigate drag reduction by surface modification. This will be done by applying an automatic optimization chain. The minimum search algorithm is based on the conjugate-gradient method [3]. By solving an adjoined equation problem it is possible to find the gradient of the cost function without the need to evaluate the flow conditions for each design variable [4]. For this purpose, a solver for the discrete adjoint equation has been implemented in the DLR TAU-code [5] and was already applied in different optimization tasks [6] [7]. In the current version of the optimization chain, the surface parameterization is realized by the Free Form Deformation technique [8], which shows to have a good shape control with relative few design variables.

To reduce the main rotor head drag, the idea is to cover parasite drag producing parts, e.g. control rods, with a hub fairing. At this place, the challenge is to find a geometry that cover the drag producing parts, without causing collision with the rotor blade movements (swiveling, flapping and pitching).

The following sections will give a short overview of the considered common H/C platform and the used optimization techniques. Additionally the results of the fuselage and main rotor optimization will be presented, before the conclusion of this study will be summarized.

Common H/C Platform

For the GRC2 project, several helicopters had been defined as reference platforms for the different optimization tasks. One of these helicopters is the common H/C platform of the GRC2 project that represents the heavy load class (take-off weight higher than 7 t) [9]. The shape is based on a 1:3881 scaled, mirrored NH90 fuselage defined in the GOAHEAD-project [10]. In Figure 1 the model and its parts are depictured. In Figure 2 the fuselage is shown in a 3-side view with its main measurements. The red dotted line shows the maximum displacement on the ramp, to ensure its functionality. An additional constraint of the current study is that the surface modification is only allowed outwards, so that the modification can

easily be realized as a retrofit for the original geometry.

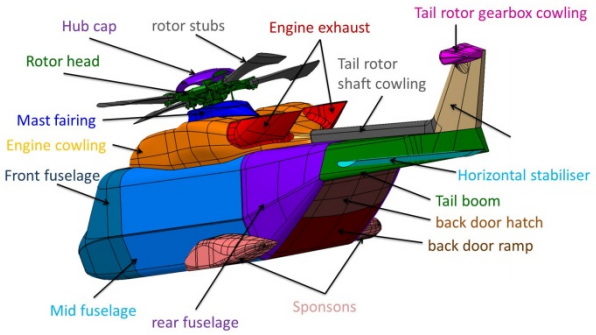

Figure 1: Common H/C Platform of the GRC2 project

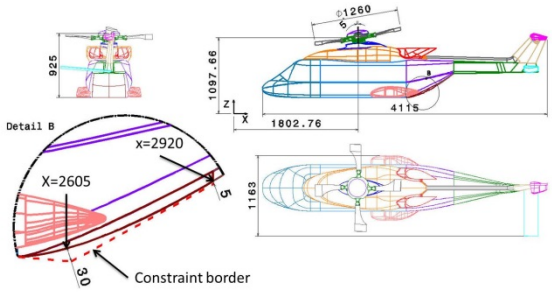

Figure 2: Common H/C Platform 3-side view

Optimization chain

The foundation of the optimization chain is the DLR TAU-code. This CFD-solver includes several tools, like an adjoint solver and a FFD module as well as a RBF module for grid deformation. For an automatic optimization of a target surface, these tools were coupled by a Python script and combined with a conjugate-gradient based optimum search. An overview of the resulting chain is given in Figure 3. This optimization chain was already successfully used with a different geometry deformation approach in the past [7]. For this investigation the surface parameterization is realized by FFD, while the grid deformation is performed by the more stable RBF deformation tool.

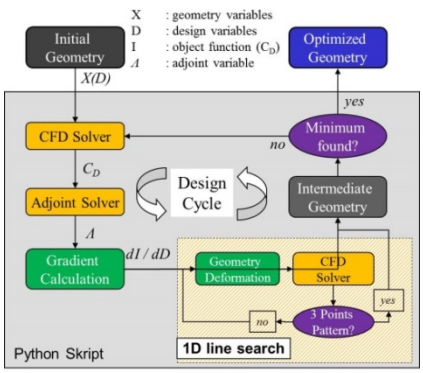

Figure 3: Optimization chain for surface drag reduction

TAU CFD-Solver

The DLR TAU-code solves the compressible Reynolds-averaged Navier-Stokes equations with a cell-vertex based finite volume discretization on hybrid grids. For the optimization task the spatial discretization is done by a central Jameson scheme. For time integration an implicit backward Euler scheme with LUSGS iteration is used. Turbulence modelling is done with the one-equation Spalart-Almaras model [11]. By using a three level multigrid, the convergence of the RANS solution could be accelerated. More detailed information to the TAU-code could be found in [12].

The Adjoint approach

For a cost function $I = I(W(D), D)$, the gradient is formulated as:

$$\frac{dI}{dD} = \frac{\partial I}{\partial D} + \frac{\partial I}{\partial W}\frac{\partial W}{\partial D} \tag{1}$$

For this investigation the cost function I is the drag coefficient. W is the vector of the flow variables that is also depending on the design variables D. To determine the sensitivity term $\partial W/\partial D$, the flow solution has to be usually computed for each design variable. For many design variables, this will get very expensive.

At this place, the adjoint approach decouples the gradient calculation of the cost function of the flow variables W. This is done by defining the Lagrangian function L as:

$$\mathrm{L} = \mathrm{I} + \Lambda^{\mathrm{T}}\mathrm{R} \tag{2}$$

R is the flow residual and is considered as very small for a convergent flow solution so that $L \approx I$. Λ is the so called Lagrangian multiplier. The gradient of the cost function can be written as:

$$\frac{dL}{dD} = \left[\frac{\partial I}{\partial D} + \frac{\partial I}{\partial W}\frac{\partial W}{\partial D}\right] + \Lambda^T\left[\frac{\partial R}{\partial D} + \frac{\partial R}{\partial W}\frac{\partial W}{\partial D}\right] \tag{3}$$

Collecting all terms with $\partial W/\partial D$ leads to:

$$\frac{dL}{dD} = \left[\frac{\partial I}{\partial W} + \Lambda^T\frac{\partial R}{\partial D}\right]\frac{\partial W}{\partial D} + \frac{\partial I}{\partial D} + \Lambda^T\frac{\partial R}{\partial D} \tag{4}$$

By setting the first bracket to zero $\partial W/\partial D$ will be eliminated. For this we obtain the so called adjoint equation:

$$-\frac{\partial I}{\partial W} = \Lambda^T\frac{\partial R}{\partial D} \tag{5}$$

By solving this linear problem, the Lagrangian multiplier Λ can be evaluated. With a known Λ, the gradient of the cost function can be simplified to:

$$\frac{dI}{dD} = \frac{dL}{dD} = \frac{\partial I}{\partial D} + \Lambda^T \frac{\partial R}{\partial D} \quad (6)$$

The remaining terms $\partial I/\partial D$ and $\partial R/\partial D$ can be approximated by finite differences.

Minimum search with conjugate-gradients

The idea of a gradient-based optimization is to move the design variables $D_k$with a step size l_s in a direction d_k, such that the cost function will be reduced:

$$\mathrm{I}(D_k + l_s d_k) \leq \mathrm{I}(D_k) \quad (7)$$

Here k is the counter of the current design cycles. In the first step, the direction d_1 will be calculated by the negative gradient of the cost function:

$$d_1 = -\nabla I(x_1) \quad (8)$$

By repeating this step for the next design cycle, the method will correspond to the steepest descent technique. The minimum search of this method can be accelerated by modifying the next search direction depending on the previous direction. This so called conjugate-gradient method was first proposed by Fletcher and Reeves [3]. Here the current direction d_k is defined as:

$$d_k = -\bar{g}_k + \beta_{k-1}\mathrm{d_{k-1}} \quad (9)$$

$\bar{g}_k$ is the current gradient of the cost function and the coefficient $\beta_{k-1}$was defined by Fletcher and Reeves as:

$$\beta_k = \frac{\bar{g}_k^T \bar{g}_k}{\bar{g}_{k-1}^T \bar{g}_{k-1}} \quad (10)$$

Another problem for this task is to choose an ideal step size l_s, that leads us to the minimum cost function along d_k. This one-dimensional minimization problem can be handled by a bracketing algorithm. Therefore a given initial step size will be modified, till a minimum of the cost function is found by a three-point pattern.

Surface Parameterization with FFD

To modify the target surface, an appropriate method of parameterisation has to be found. A good possibility for this is to use the Free Form Deformation technique. The advantages of this method are that it is possible to achieve a global control of the surface with relatively few design variables. This is done by defining a deformation box with $\vec{Q}_{i,j,k}$ control points. All points of the target surface will then be mapped in a B-spline volume:

$$\vec{\mathrm{P}}_\mathrm{I} = \sum_{\mathrm{i=0}}^{\mathrm{nu}} \sum_{\mathrm{i=0}}^{\mathrm{nv}} \sum_{\mathrm{i=0}}^{\mathrm{nw}} \mathrm{N_{i,m_u}(u) N_{i,m_v}(v) N_{i,m_w}(w) \vec{Q}_{i,j,k}} \quad (11)$$

The point location (u_I, v_I, w_I) for each surface point $\vec{P}_I$ is evaluated by a Newton iteration method. The next step is to modify the B-spline volume by changing the control points $\vec{Q}_{i,j,k}$ to $\vec{R}_{i,j,k}$:

$$\vec{P}_{I,new} = \sum_{i=0}^{nu} \sum_{i=0}^{nv} \sum_{i=0}^{nw} N_{i,m_u}(u) N_{i,m_v}(v) N_{i,m_w}(w) \vec{R}_{i,j,k} \quad (12)$$

Now the point location (u_I, v_I, w_I) will be re-mapped to the Cartesian coordinate system by using the new B-spline volume. In Figure 4 the FFD steps are illustrated. For further information the reader is referred to [8].

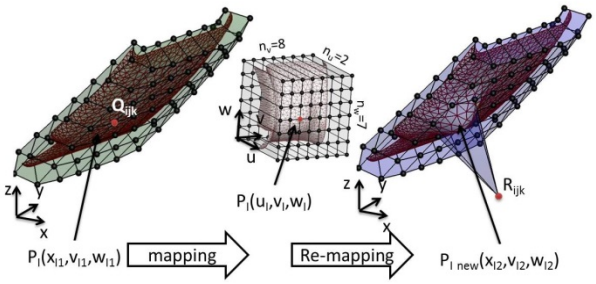

Figure 4: Principle steps of FFD

Grid Deformation with RBF

FFD is a good possibility to deform surface geometries. For CFD application the surrounding mesh, that discretises the considered control volume, has to be adapted to the new surface. A good method for this is the deformation by Radial Base Function. For this investigation a classic volume spline was used as Radial Base Function:

$$\Delta x(x,y,z) = f(wd)(\alpha_1 + \alpha_2 x + \alpha_3 y + \alpha_4 z) \quad (13)$$
$$+ \sum_i^N \beta_i \sqrt{(x-x_i)^2 + (y-y_i)^2 + (z-z_i)^2})$$

$f(wd)$ is a weight function depending on the wall distance. This way it is possible to control the abate rate of the deformation in space. By specifying base points with a given Δx as scattered data, the coefficients α_i and β_i can be interpolated by solving the following set of linear equations:

$$\Delta \underline{x} = \bar{\bar{A}} \begin{pmatrix} \underline{\alpha_x} \\ \underline{\beta_x} \end{pmatrix}, \ \Delta \underline{y} = \bar{\bar{A}} \begin{pmatrix} \underline{\alpha_y} \\ \underline{\beta_y} \end{pmatrix}, \ \Delta \underline{x} = \bar{\bar{A}} \begin{pmatrix} \underline{\alpha_z} \\ \underline{\beta_z} \end{pmatrix} \quad (14)$$

A disadvantage is that the interpolation matrix $\bar{\bar{A}}$ has the dimension $N \times N$, where N is the number of base points. This means that with many base points, the required inversion of $\bar{\bar{A}}$ gets very expensive. The advantage of this method is that it

is not necessary that the given base points match exactly the grid points of the CFD-mesh that have to be deformed. This way it is possible to reduce the base point number without reducing the point number of the CFD-grid. Additionally the implemented RBF-module in TAU provides a base point reduction algorithm to ensure that a given number of points will not be exceeded.

The deformation algorithm of the optimization chain

In Figure 5 the principle steps of the used deformation algorithm are shown. At the beginning the initial CFD-grid is given. The first step will be to create a surrogate mesh that includes the target surface of the CFD-grid (red). The target surface of the surrogate mesh will then be surrounded by a deformation box with the dimension $N \times M \times 2$. To keep the connectivity with the surrounding surfaces, the outer control points are fixed. Further, only the outboard laying control points will be moved in the normal direction of the target surface. This way, and because of symmetry reasons the number of design variables can be calculated as:

$$(N-1)\cdot\left(\frac{M-1}{2}\right) \qquad (15)$$

The second step is to deform the target surface by manipulating the control points of the FFD-box. After this, the resulting displacement of the surrogate grid points are calculated, by subtracting the initial coordinates from the deformed coordinates. This provides the required scattered data for the RBF-deformation of the computational mesh. The new CFD-grid will then be used as initial grid for the next design cycle of the optimization chain.

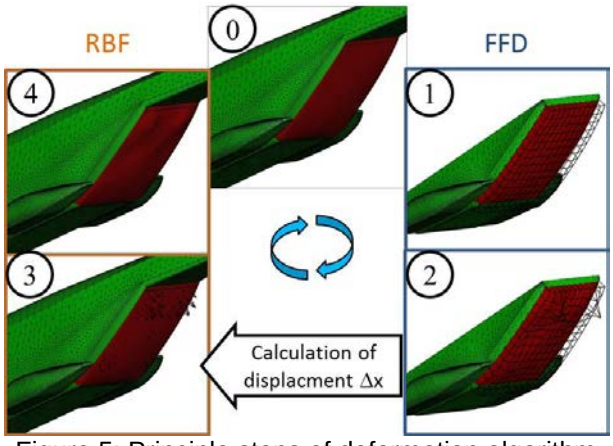

Figure 5: Principle steps of deformation algorithm

Optimization run

Setup

The optimization task was done at cruse flight conditions. The remaining parameters are summarized in Table 1. The volume mesh was created with Pointwise [13]. It contents about 3.3 million points and the fuselage surface is covered by 30 prism layer to resolve the boundary layer (see Figure 6(a)). The initial height of the prism layer is 0.008mm. The wake region behind the engine exhausts and the back door were discretized by a finer mesh to ensure a sufficient resolution of the accruing vortices.

As the unsteady wake behind the engine exhausts causes problems to the adjoint solver, a second, simplified grid was used for the optimization cycles (see Figure 6(b)). All superstructures, the tail fin and the horizontal stabilizer were removed as their influence on the back door flow is considered small. The resolution of the boundary layer was left unchanged. The resulting grid has about 1.3 million points left.

To start the optimization chain, an initial flow solution with 50000 iterations was performed with the one equation Spalart Allmaras turbulence model. The adjoint solution was performed with 10000 iterations. The Krylov subspace method GMRes [14] was applied with 50 inner iterations to stabilize the calculation. During the optimization cycles, the flow solution as well as the adjoint solution was recomputed with 10000 iterations. An overview of the major input parameter for the optimization chain is given in Table 2.

For the Free Form Deformation, a third grid was generated, to keep the computational costs for the deformation steps low. Figure 7 shows the surrogate grid, which includes the target surface (red), the rear fuselage part, the sponsons and a piece of the middle fuselage. The surrounding surfaces of the target surface are needed to ensure a smooth connection at the borders.

Figure 7 shows additionally the deformation box for 32 design variables (see eq (15)). In this investigation, three different boxes with 15, 32 and 65 design variables were used to investigate the influence of the design variable number. The boxes were generated, by extruding the target surface in normal direction with 80mm outwards and 20mm inwards.

To ensure, that the optimized surface doesn´t penetrate inside the original model, only outwards deformation of the deformation box were allowed. The given constraints on the back door ramp were realized by limiting the maximum displacement vector of the RBF scattered data to the given values.

In case, that the surface deformation is too strong for the grid deformation, a penalty value is given to the drag value, to avoid that the optimizer stops by destroying the calculation grid.

After the optimization chain delivers an optimized shape, the result is verified by recalculating the flow conditions with the original grid by using the Wilcox-κ-ω-turbulence model [15]. Additionally a polar within the range of α=-10° to α=10° is calculated to investigate the benefits for different pitch angles. The modified surface is applied to the full model by RBF-deformation with the scattered data provided by the optimization chain.

Table 1: cruise flight conditions

Ma [-]	Re[-]	ρ [kg/m^3]	T [K]	α[°]	ref. area
0.204	4.1e6	1.225	288.15	-1.8°	1m^2

Table 2: parameter of the optimization chain

Ini. flow iter.	Ini. adjoint iter.	flow iter.	adjoint iter.
50000	10000 (50GMRes)	10000	10000 (50GMRes)
No. of Design variables	Defo. Norm. value	Ini. step size	Turb. Model
15, 32, 65	0.001	0.01	SA

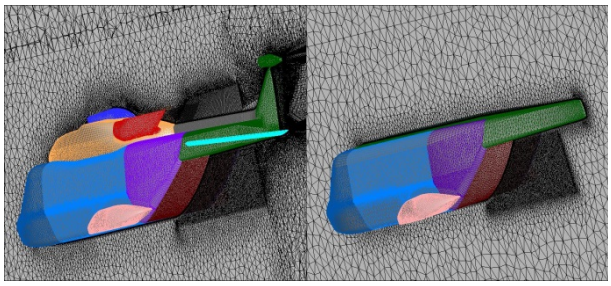

(a) original (b) simplified

Figure 6: Computational grids for CFD

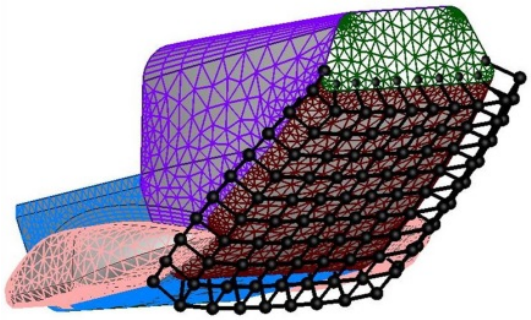

Figure 7: surrogate grid with FFD-box

Results of the optimization

The convergence behavior of the three optimization runs with different number of design variables is plotted in Figure 8. The ΔC_d-values that hit exactly 0%, corresponds to the penalty value for grid destruction. It can be seen that the maximum drag reduction of 4.48% could be achieved with 65 design variables. Though during this computation, the grid was destroyed several times by too large surface deformations. The maximum drag reduction found decreases with the number of design variables. With 15 design variables, the minimum is already found after several cycles, while for the remaining cycles, the cost function keeps rising till its stabilize to a of nearly 0%.

Figure 9 illustrates the optimized surfaces for all three test cases, compared with the baseline configuration. In all cases, the optimizer pulls out two small bumps on the back door ramp and two higher bumps on the hatch. The case with 32 design variables contains the highest deformation. At this place it can be observed, how the constraints limit the propagation of the bumps on the back door ramp. The optimization run with 65 design variables forms two similar bumps on the hatch. Here the top of the bumps are smaller and situated a bit further downstream. The parameterization with 15 design variables wasn´t able to pull out the surface as far as the two other cases.

Figure 10 shows the skin friction for all configurations. Additionally two contiguous cuts with the $\lambda 2$ criteria at x=3.2m and x=3.6m were done, to illustrate the trailing vortices. This way it can be seen, how the drag reduction is achieved on the simplified model. The baseline shows a area of separated flow on the back door hatch (green). Additionally two strong trailing vortices are formed outside and two weaker, counter rotating vortices are induced near the middle line. Compared to the baseline, the solution with 65 design variables pushes the beginning of the separation area backwards, while the end of this region is situated a bit further downstream on the tail surface. Further, the modified surface reduces the size of the outer vortices. This effect can also be observed for the results with 32 design variables. But in this case, the separation area couldn´t be reduced as much as for the version with 65 design variables. The optimization with 15 design variables is able to reduce the separation area slightly, compared to the baseline. However this reduction is achieved to the costs of two stronger inner vortices. The outer vortices remain nearly unaffected.

Comparing these results of the simplified model with the flow on the full model, some differences can be observed (see Figure 11). The separation area on the back door is predicted larger compared to the simplified model. The solution with 65 design variables additionally show larger inner vortices, while the surface with 32 design variable causes one large and one small inner vortex, that dissipate quite fast to the second cut. In both cases, a back flow region (green) appears in front of the large bumps, were the geometrical constrains obstruct the deformation. These

differences in the prediction are mainly caused by the different turbulence model and the simplified grid.

Having a look on the drag breakdown of the full model, it can be observed that the maximum drag reduction is found with 1.41% on the optimized surface with 32 design variables. The first reason for this lower value is that for the full model, the reference drag coefficient of the baseline is higher than for the simplified model. Additionally, the differences in the flow prediction, as described before, cause a higher drag force, especially for the case with 65 design variables. This case has the largest drag reduction on the back door itself, but the version with 32 design variables show better benefits on the stabilizer, sponsons and the rear fuselage. The modification with 15 design variables show with a reduction of 0.8% only small influences on the total drag.

The comparison of the drag over pitch angle curves shows an augmentation of the relative drag reduction at low pitch angles (see Figure 13). For the modification with 65 design variables, a minimum of 3.75% could be found at $\alpha = -8°$. For positive pitch angle higher than $\alpha = 2.5°$, the drag of the optimized surface gets larger compared to the baseline and has a maximum drag increase of -3.35% at $\alpha = 8°$. The curve of relative drag reduction of the solution with 15 design variables has a similar trend. But compared to the curve with 65 design variables, the maximum values are smaller. The largest drag reduction is found at $\alpha = -6°$ with 1.76% and the highest drag increase is found at $\alpha = 8°$ with -1.06%. The trend of the 32 design variable curve is quite unsteady. For this case, a relative drag reduction could only be found between $\alpha = 0°$ and $\alpha = -5°$. For higher or lower pitch angle, the drag is increased by the modified surface and has a maximum of -3.15% at $\alpha = 10°$. Over all, the solution with 65 design variables seems to be the best solution for forward flight conditions, as the benefits rises by pitching down the nose, which corresponds to the manoeuvre to accelerate the helicopter.

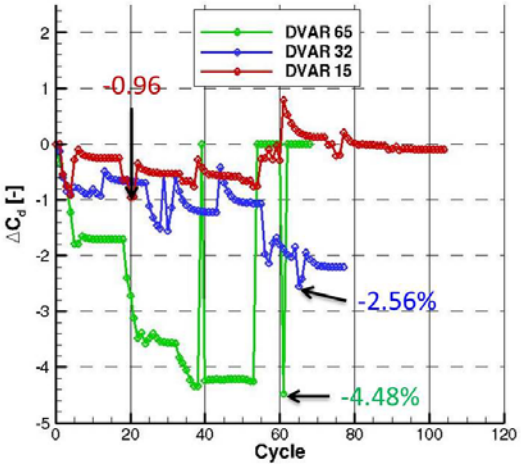

Figure 8: Convergence behaviour of the optimsation runs

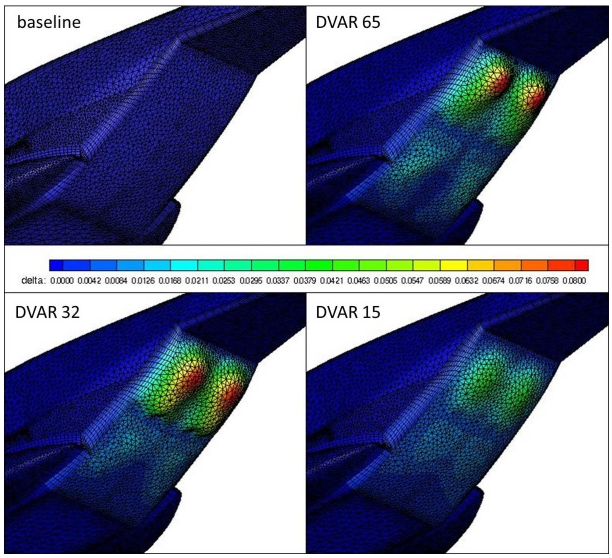

Figure 9: optimized surface deformation of the simplified model

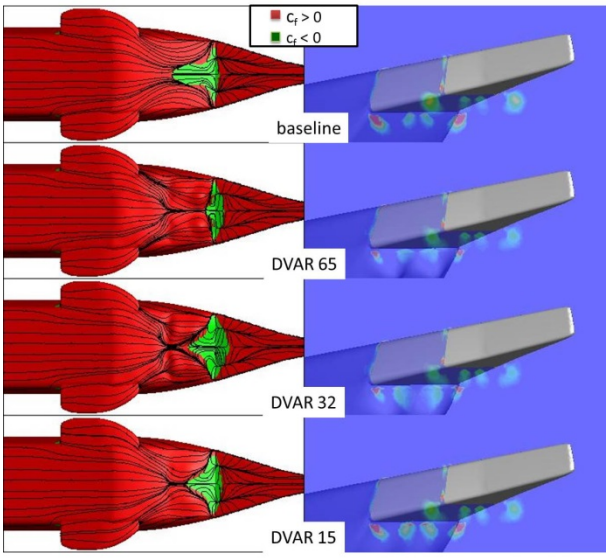

Figure 10: skin friction and λ2 cuts of the simplified model

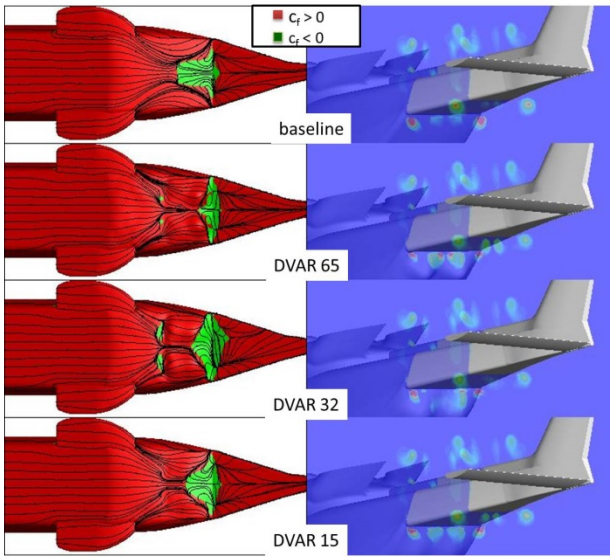

Figure 11: skin friction and λ2 cuts of the full model

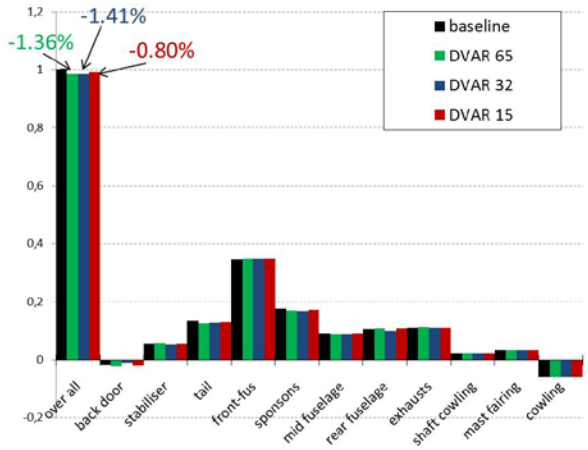

Figure 12: Drag breakdown for the verification calculations

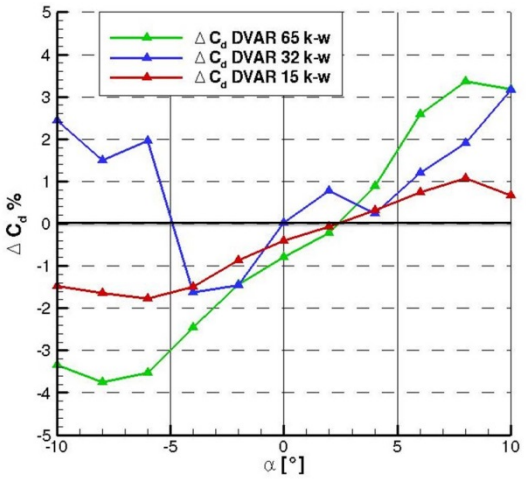

Figure 13: Relative drag reduction by back door optimization with respect to baseline configuration

Hub optimization

The second approach applied to improve helicopter drag characteristics relied on manual optimization of rotor hub drag and the minimization of its mutual interference with the fuselage. Several ideas have been proposed and tested, such as application of full hub fairing, mast fairing streamlining to reduce the local dynamic pressure experienced by the hub, and the inclusion of the hub in the wakes of mini spoilers mounted on the top of the fuselage. Many of these techniques proved to be inefficient to cause a worthy improvement owing to domination of rotor downwash on the upper side of the fuselage. In this paper the most promising approach will be highlighted, namely the full fairing.

Baseline and proposed configurations

All configurations reported in this paper feature the GRC common H/C platform [9] fuselage and a stationary rotor hub. Two different full fairing designs were selected for comparison with the baseline hub specified for the common H/C platform. The results also include data of one streamlined mast fairing. The rotor is not considered in the reported investigation since its effects were qualitatively irrelevant to the configurations considered here. This has been revealed by other results where the rotor effects were taken into account by an actuator disc model. These results are not shown here due to space limitations.

Figure 15 compares the geometry and surface grid of the baseline rotor hub and the two proposed full fairings. The first full fairing, denoted FF-V3, features exposed blade stubs, a flat base and a blended convex-concave upper surface. The second full fairing, FF-V5, featured a raised belt line and blended streamlined blade stubs. In Figure 16 the surface model of the baseline and the modified mast fairing are shown.

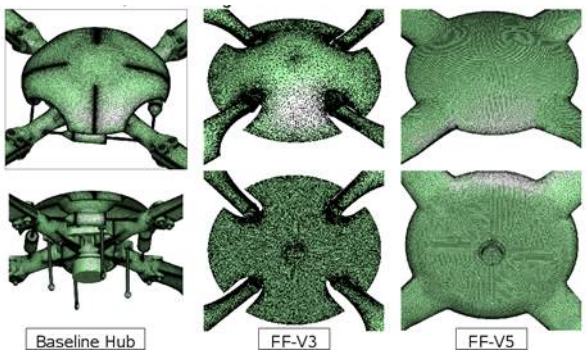

Figure 14: Surface grid of fairing versions

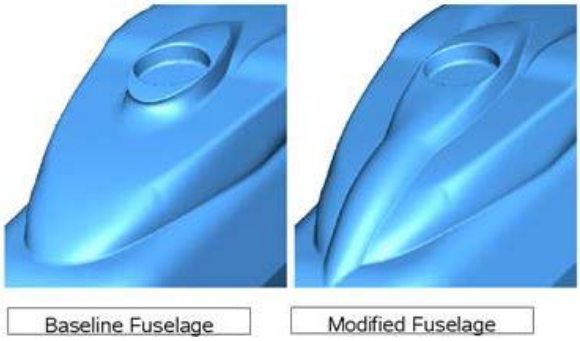

Figure 15: Baseline and modified mast fairing

Computational setup

The numerical results were obtained by solving the Reynolds-averaged Navier-Stokes equations in three dimensions using the DLR TAU-code and unstructured grids. Turbulence effects are taken into account by Wilcox's two-equation k-ω model. An overview of the flow conditions is given in Table 3. Unstructured grids were generated around the individual components with the grid generator CENTAUR [16], and combined by the overlapping grid technique Chemira to build the desired configuration (see Figure 17). The grids of the two fuselage variants consist of about 7.3 million points each. The baseline rotor head mesh includes about 23 million points, while the full fairing FF-V3 and FF-V5 have 5.8 and 7.6 million points respectively.

Table 3: Parameter of the CFD computation

Ma [-]	Re[-]	α[°]	Turb. Model
0.204	4.1e6	-15°:15°	Wilcox κ-ω

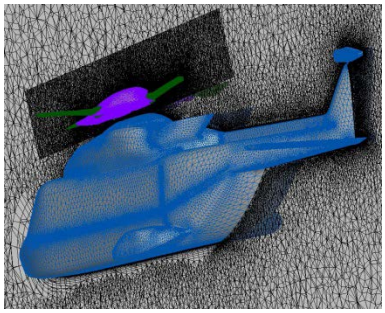
Figure 16: Baseline fuselage grid + FF-V3 hub grid

Results

In Figure 18 the total drag coefficient is plotted over the pitch angle. It can be seen that in the full range of $-15° < \alpha < 15°$, the fairing version FF-V3 in combination with the baseline fuselage results in a benefit of 3 to 5%. By employing the modified fuselage V4, an additional improvement of -1.5-1.9 % could be achieved in the range $-5° < \alpha < 5°$. The hub and stub fairing design FF-V5 combined with the baseline fuselage brings a drag reduction of about 17.7 to 19.2%.

The drag polar shown in Figure 19 for the complete configuration reveals a nearly symmetric behaviour of drag benefit about a mean C_l value for the FF-V3 fairing plus the modified fuselage V4 configuration. The best drag gain for this configuration was about 5%, which is almost 1.5% less than the baseline fuselage combined with the same fairing. The drag benefit vanishes almost completely with higher lift coefficients, and diminishes with decreasing C_l, becoming finally negative -2% (drag increase) at very low C_l values. By applying the V5 fairing to the baseline fuselage, a maximum benefit of almost 25% could be achieved, as this configuration does not only reduce the drag but also increase the lift.

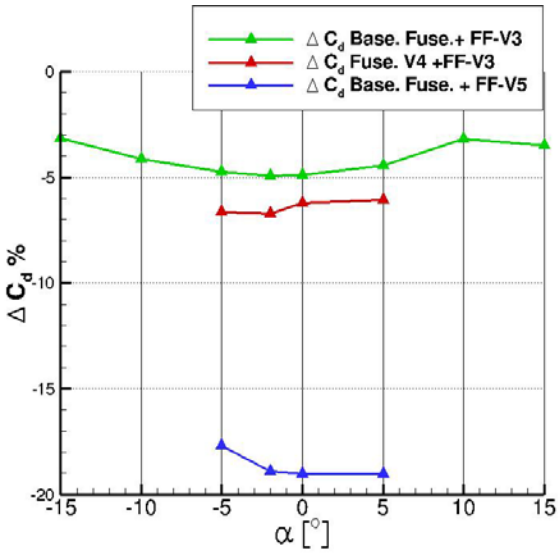

Figure 17: Relative drag reduction of rotor head modification with respect to baseline configuration

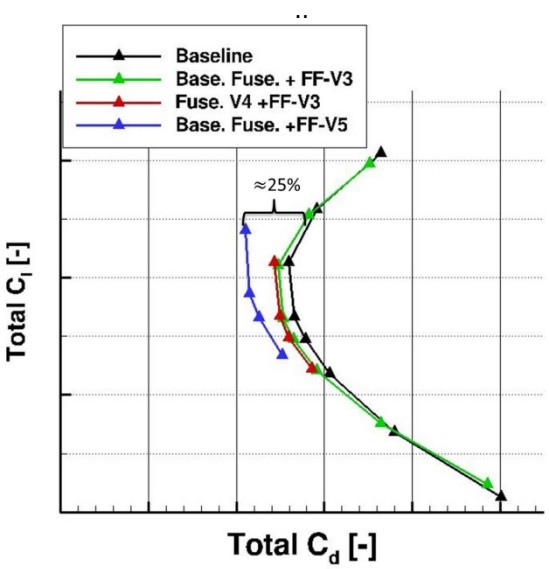

Figure 18: Drag polars of the baseline and modified fuselage V4 combined with different hub fairing shapes

Conclusions

During this study, two different approaches were applied to reduce the parasite drag of a heavy

transport helicopter. The first approach was to modify the back door surface with an automatic optimization chain. This chain couples several applications, like a CFD-solver and an adjoint-solver in a python environment. The surface parameterisation was done by FFD and the optimization algorithm is based on conjugate gradients. The optimization task was performed with three different numbers of design variables. Because of the sensitivity of the adjoint solver to unsteady flow conditions, and to reduce the total computational costs, a simplified geometry was used for the optimization calculations along with the Spalart-Allmaras turbulence model. As expected, the optimization with the highest number of design variables returns the best result, while the resulting deformations are close to the limits of RBF-deformation. A verification calculation of the optimized surface with the full model and the Wilcox κ-ω turbulence model rectified the predicted relative drag reduction to lower values. Nevertheless, a total drag reduction of 1.41% for the design pitch angle and a benefit of 3.75% at $\alpha = -8°$ could be achieved. This is due to the repression of the separation area by two bumps on the back door hatch. Additionally the two outer trailing vortices could be reduced, to the cost of stronger inner vortices. The optimized surface also managed to reduce the outer trailing vortices, but to the cost of stronger inner vortices. The next step will be to apply the optimization chain to the sponsons of the common H/C platform. Additionally the optimization chain will be tested with different turbulence models.

The second approach to reduce parasite drag, was the application of main rotor hub fairing. The possibility to reduce the mutual hub-fuselage interference by streamlining the mast fairing was also investigated. As the results indicate, the latter approach was not as effective as the preliminary results indicated. The most successful fairing design with exposed stubs resulted in an improvement of about 6.6% of total drag. The possibility to reduce the drag further by using streamlined stub fairings was also examined. It could be shown that by covering the blade stub in addition to the hub, a remarkable improvement of the total drag between 17.7-19% could be obtained. Evaluation of the drag data at constant lift conditions reveals an improvement between 13 and 23% of total drag.

References

[1] Proudy, R. W., “Helicopter Performance, Stability, and Control” PWS Engineering, ISBN:0534063608, 9780534063603 University of Michigan, 1986

[2] Boniface, J.-C., Joubert, G., Le Pape, A., “Passive Flow Control by Vortex Generators of Internal and External Aerodynamics Configurations”, 48th International Symposium of Applied Aerodynamics Saint-Louis, 25-27 March 2013

[3] Fletcher, R., Reeves, C. M., “Function Minimization by Conjugate Gradient”, Computer Journal., 7, 149-154, 1964

[4] Jameson, A., Martinelli, L., “Aerodynamic Shape Optimisation Techniques Based on Control Theory”, CIME (International Mathematical Summer Center), Martina Franca, Italy, 1999

[5] Dwight, R.P., “Efficiency Improvements of RANS-Based Analysis and Optimization using Implicit and Adjoint Methods on Unstructured Grids”, Ph.D. thesis, University of Manchester, Manchester, UK, 2006

[6] Brazillon, J., Dwight, R. P., “Aerodynamic Shape Optimisation using the Discrete Adjoint of the Navier-Stokes Equations: Applications towards Complex 3D Configurations”, Proceeding of the CEAS/KATnet II Conference on Key Aerodynamic Technologies, Paper No. 36-1, May 2009

[7] Q.Zhang, J.-H. Wendisch, J.-D.Lee, „An Adjoint-Based Optimisation Method for Helicopter Fuselage Backdoor Geometry“, 36th European Rotorcraft Forum 2010, 7.-9. Sep. 2010, Paris, France

[8] Segerberg, T. W., Parry, S. R., “Freeform Deformation of Solid Geometric Models”, Proceedings of SIGGRAPH 1986, Dallas, USA, Aug. 18-22, 1986

[9] D´Alascio, A., Kneitsch, T., “Specification of Geometrical Constrains and of the Design Points for Common Helicopter Platform Optimization Subtasks”, CSJU/ITD GRC/RP/2.2.2/32024, 2011

[10] Palke, K. “The GOAHEAD Project” 33rd European Rotorcraft Forum, Kazan, Russia, 2007

[11] Spalart, P., Allmaras, S., “A One-Equation Turbulence Model for Aerodynamic Flows”, AiAA Paper 92-0439, 1992

[12] Gerold, T., Friedrich, O., Evan, J., Galle, M., “Calculation of Complex Three-Dimensional Configurations Employing

the DLR-TAU-Code", AiAA paper 167, 1997

[13] *POINTWISE USER MANUAL.* Forth Worth, Texas, USA , s.n., 2012.

[14] Saad Y., Schultz, M.H., "GMRES: A Generalized Minimal Residual Algorithm for Solving Nonsymmetric Linear Systems", SIAM J. Sci. Stat. Comput., 7:856-869, 1986

[15] Wilcox, D.C., "Reassessment of the Sale-Determining Equation for Advanced Turbulence Models", AiAA Jounal, 26(11):1299-1310, 1988

[16] CENTAURSoft, https://www.centaursoft.com [05.02.2014]